THE JOURNAL OF PHYSICAL CHEMISTRY B

Article

pubs.acs.org/JPCB

Terms of Use

Activity and Architecture of Pyroglutamate-Modified Amyloid-β ($A\beta_{pE3\text{-}42}$) Pores

Alan L. Gillman,[†,#] Hyunbum Jang,[§,#] Joon Lee,[‡] Srinivasan Ramachandran,[†,‡] Bruce L. Kagan,[∥] Ruth Nussinov,[§,⊥] and Fernando Teran Arce*[,†,‡]

[†]Department of Bioengineering, University of California, San Diego, 9500 Gilman Drive, La Jolla, California 92093, United States

[‡]Department of Mechanical and Aerospace Engineering and Material Science Program, University of California, San Diego, 9500 Gilman Drive, La Jolla, California 92093, United States

[§]Cancer and Inflammation Program, National Cancer Institute at Frederick, Leidos Biomedical Research, Inc., Frederick National Laboratory for Cancer Research, Frederick, Maryland 21702, United States

[∥]Department of Psychiatry, David Geffen School of Medicine, Semel Institute for Neuroscience and Human Behavior, University of California, 760 Westwood Plaza, Los Angeles, California 90024, United States

[⊥]Department of Human Molecular Genetics and Biochemistry, Sackler School of Medicine, Tel Aviv University, Tel Aviv 69978, Israel

Supporting Information

ABSTRACT: Among the family of Aβ peptides, pyroglutamate-modified Aβ ($A\beta_{pE}$) peptides are particularly associated with cytotoxicity in Alzheimer's disease (AD). They represent the dominant fraction of Aβ oligomers in the brains of AD patients, but their accumulation in the brains of elderly individuals with normal cognition is significantly lower. Accumulation of $A\beta_{pE}$ plaques precedes the formation of plaques of full-length Aβ ($A\beta_{1\text{-}40/42}$). Most of these properties appear to be associated with the higher hydrophobicity of $A\beta_{pE}$ as well as an increased resistance to enzymatic degradation. However, the important question of whether $A\beta_{pE}$ peptides induce pore activity in lipid membranes and their potential toxicity compared with other Aβ pores is still open. Here we examine the activity of $A\beta_{pE}$ pores in anionic membranes using planar bilayer electrical recording and provide their structures using molecular dynamics simulations. We find that $A\beta_{pE}$ pores spontaneously induce ionic current across the membrane and have some similar properties to the other previously studied pores of the Aβ family. However, there are also some significant differences. The onset of $A\beta_{pE3\text{-}42}$ pore activity is generally delayed compared with $A\beta_{1\text{-}42}$ pores. However, once formed, $A\beta_{pE3\text{-}42}$ pores produce increased ion permeability of the membrane, as indicated by a greater occurrence of higher conductance electrical events. Structurally, the lactam ring of $A\beta_{pE}$ peptides induces a change in the conformation of the N-terminal strands of the $A\beta_{pE3\text{-}42}$ pores. While the N-termini of wild-type $A\beta_{1-42}$ peptides normally reside in the bulk water region, the N-termini of $A\beta_{pE3\text{-}42}$ peptides tend to reside in the hydrophobic lipid core. These studies provide a first step to an understanding of the enhanced toxicity attributed to $A\beta_{pE}$ peptides.

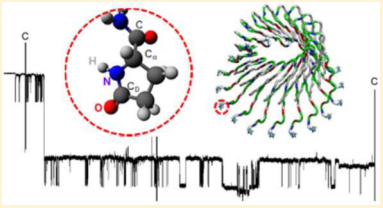

INTRODUCTION

The amyloid hypothesis states that accumulation of amyloid-β (Aβ) peptides in the brain is the primary driver of pathogenesis in Alzheimer's disease (AD), including synapse loss and neuronal cell death.[1] The full-length $A\beta_{1\text{-}42}$ peptide and its $A\beta_{17-42}$ fragment (p3) are formed via cleavage of the amyloid precursor protein (APP) by the action of three secretase enzymes.[1b,2] The $A\beta_{pE3\text{-}42}$ fragment is post-translationally generated by cleavage of the first two N-terminal amino acids of $A\beta_{1\text{-}42}$, leaving an exposed glutamate (E) residue in position 3. The lactam ring in the pyroglutamate (pE) residue is subsequently generated by intramolecular dehydration catalyzed by the glutaminyl cyclase (QC) enzyme.[3]

pE-modified Aβs represent the dominant fraction of Aβ oligomers in brains of AD patients.[3] Autopsied brains of elderly patients with normal cognition also show accumulation of $A\beta_{1\text{-}40/42}$, but the amount of accumulated $A\beta_{pE3\text{-}42}$ is significantly lower.[4] Consequently, the ratio of $A\beta_{pE3\text{-}42}/A\beta_{1\text{-}42}$ oligomers is higher in AD brains than in brains of normal elderly individuals.[3,4] The larger accumulation of $A\beta_{pE3\text{-}42}$ in AD brains has been attributed to its increased stability and higher aggregation propensity.[3] These properties are attributed to the lactam ring in the pE-modified third residue as well as the loss of electrical charge in three residues during the conversion of $A\beta_{1\text{-}42}$ to $A\beta_{pE3\text{-}42}$, thus resulting in higher $A\beta_{pE3\text{-}42}$ hydrophobicity and increased resistance to degradation by peptidases.[3] Significantly, it is also believed that the formation of $A\beta_{pE3\text{-}42}$ plaques precedes $A\beta_{1\text{-}40/42}$ plaque formation.[3b] This is supported by the observation that $A\beta_{pE3\text{-}42}$ plaques appear earlier than $A\beta_{1\text{-}40/42}$ plaques in Down syndrome (DS) brains.[3] The additional copy of chromosome 21, characteristic of DS, is

Received: April 27, 2014
Revised: June 10, 2014
Published: June 12, 2014

 © 2014 American Chemical Society dx.doi.org/10.1021/jp5040954 | J. Phys. Chem. B 2014, 118, 7335−7344

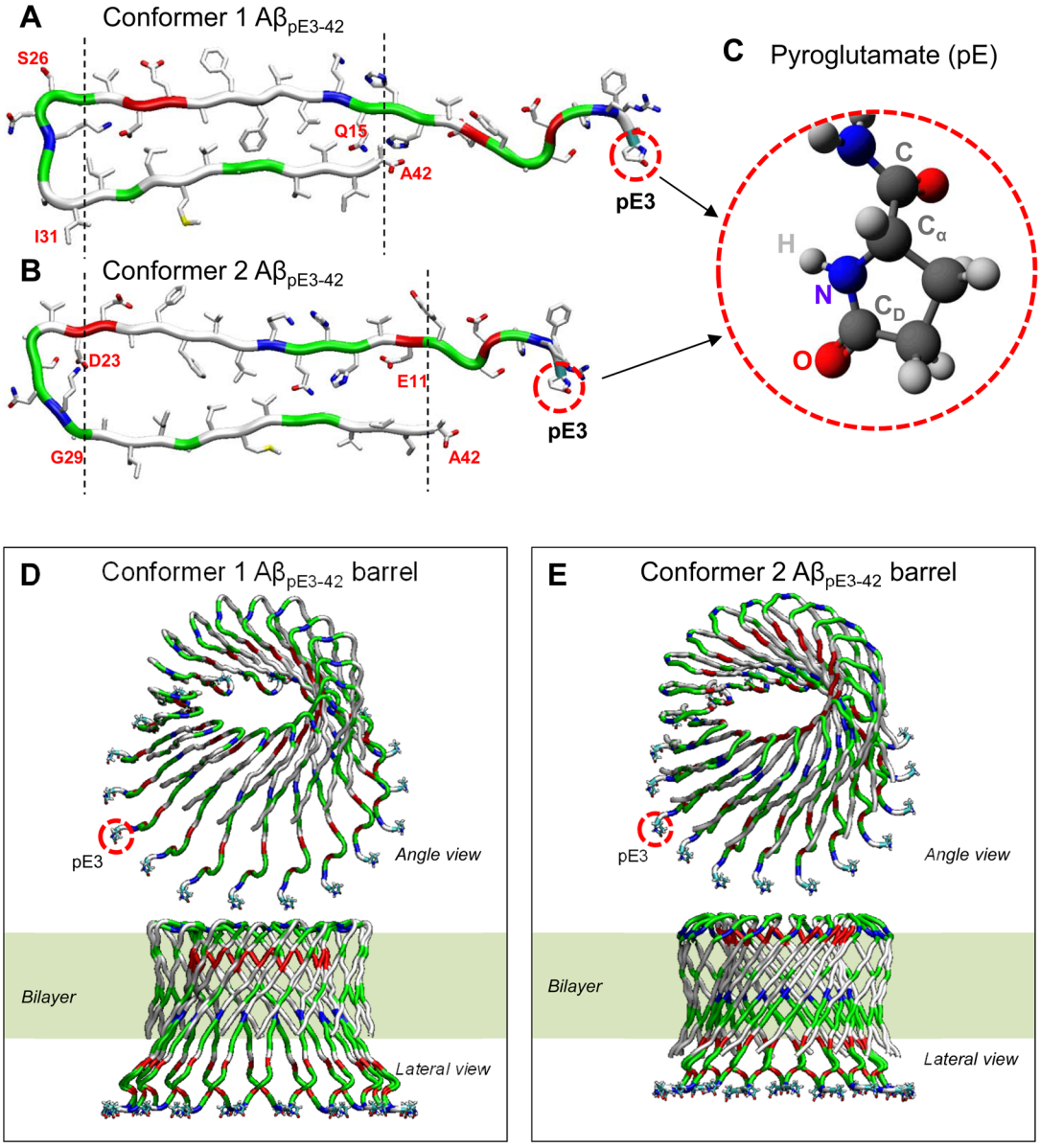

Figure 1. Monomer conformations of (A) conformer 1 $A\beta_{pE3-42}$ with turn at Ser26-Ile31 and (B) conformer 2 $A\beta_{pE3-42}$ with turn at Asp23-Gly29, and (C) highlight of pyroglutamate at residue 3 (pE3). Dotted lines on the monomer structures denote the locations of bilayer surfaces. The initial barrel structures of MD simulations in ribbon representation for the (D) conformer 1 and (E) conformer 2 $A\beta_{pE3-42}$ barrels. In the peptide ribbon, hydrophobic, polar/Gly, positively charged, and negatively charged residues are colored white, green, blue, and red, respectively. The pE3 N-terminal termini are highlighted as threads.

responsible for generating more APP, and thus individuals with DS are more likely to develop AD earlier in life.[1a]

Increasing evidence suggests that following initial interactions on the cell membrane, $A\beta$ oligomers insert into the membrane and form pore structures.[5] Cell toxicity results from an abrupt change in cell ionic concentration, producing loss of cell homeostasis. Pore activity has been observed for full-length $A\beta$s,[5a,b,6] $A\beta$ fragments,[2b,7] and point substitutions.[2b,8] In addition to pore formation, $A\beta$-induced toxicity mechanisms include lipid extraction by peptides on the membrane surface.[9] These mechanisms are not mutually exclusive, as a recent study suggested that pore formation precedes nonspecific fragmentation of the lipid membrane during amyloid fiber formation.[10]

To the best of our knowledge, there is currently no experimental data for amyloid pore formation in vivo. $A\beta_{pE3-42}$ was observed to induce neurodegeneration and lethal neurological deficits in transgenic mice.[11] These $A\beta_{pE3-42}$ mice displayed a significantly reduced survival rate compared with $A\beta_{1-42}$ transgenic mice.[11] In vitro, optical patch-clamping was used to characterize the single-channel Ca^{2+} fluorescence transients induced by $A\beta_{1-42}$ pores in membranes of *Xenopus laevis* oocytes.[5e] However, most experimental evidence of amyloid pore formation stems from model membrane studies.

Here we characterize the electrical properties of pE-modified $A\beta$ in lipid membranes. We discuss the activity and structure of $A\beta_{pE3-42}$ pores in anionic model cell membranes. We used phosphoethanolamine (PE) and phosphoserine (PS) lipid headgroups to mimic the brains of elderly patients. Phospholipids with ethanolamine (PE) head groups are one of the dominant components in the brains of the elderly,[12] and these levels, as well as those of PS,[13] have been found to change in AD brains.[14] Using planar lipid bilayer (PLB) electrical

dx.doi.org/10.1021/jp5040954 | J. Phys. Chem. B 2014, 118, 7335−7344

recording, we show that $A\beta_{pE3-42}$ induces pore activity in anionic membranes, producing increased membrane permeability with respect to $A\beta_{1-42}$ pores. Using atomistic molecular dynamics (MD) simulations, we model the architecture of $A\beta_{pE3-42}$ pores and correlate them with the activity observed experimentally.

MATERIALS AND METHODS

Materials. $A\beta_{pE3-42}$ was purchased from Bachem (Torrance, CA), and $A\beta_{1-42}$ was purchased from Bachem and Anaspec (Fremont, CA). The phospholipids 1,2-dioleoyl-*sn*-glycero-3-phosphoserine (DOPS) and 1-palmitoyl-2-oleoyl-*sn*-glycero-3-phosphoethanolamine (POPE) were purchased from Avanti Polar Lipids (Alabaster, AL). All other chemicals were purchased from Sigma-Aldrich (St. Louis, MO).

Peptide Handling. $A\beta_{pE3-42}$ and $A\beta_{1-42}$ peptides were dissolved in Milli-Q water to a concentration of 1 mg/mL prior to being aliquoted for storage. These 50 μL aliquots were stored at −80 °C for a maximum of 60 days before use. Samples were thawed only once.

Planar Lipid Bilayer Electrical Recording. We prepared PLBs using the so-called "painted" technique.[15] Bilayers were formed from a 1:1 (w/w) mixture of DOPS and POPE in heptane at a total lipid concentration of 20 mg/mL. Spontaneous membrane formation occurs following the addition of lipid directly over a pore with a diameter of ∼250 μm in a Delrin septum (Warner Instruments, Delrin perfusion cup, volume 1 mL). In previous studies, this membrane composition was shown to be stable for long recording times (∼4 h).[16] As the electrolyte, we use 150 mM KCl, 10 mM HEPES (pH 7.4), and 1 mM $MgCl_2$.

Before performing electrical recordings, we verified that the bilayer was stable for several minutes with low conductance (<10 pS) across ±100 mV applied voltage and that the system capacitance was >110 pF. When both criteria were met, peptide was added directly to the cis (hot wire) side and stirred for 5 min. Peptide concentration in the bilayer chamber was ∼10 μM. Bilayer stability was monitored by periodic capacitance measurements throughout the course of the experiment.

All traces were recorded in voltage clamp mode using the 2 kHz built-in filter cutoff of our BC-535 amplifier (Warner Instruments, Hamden, CT). A sampling frequency of 15 kHz was used for all data acquisition. We used a custom-made LabVIEW program to record the current and Clampfit 10.2 (Molecular Devices, Sunnyvale, CA) to analyze traces. For representation in Figures, we have filtered the recorded current versus time traces with a digital Gaussian low-pass filter with a cutoff frequency of 50 Hz.

Atomistic Molecular Dynamics Simulations. Two U-shaped Aβ monomer conformations with the β-strand-turn-β-strand motif were extracted from $A\beta_{1-42}$ fibrils, where the structure was defined by hydrogen/deuterium-exchange NMR data, side-chain packing constraints from pairwise mutagenesis, ssNMR and EM (PDB code: 2BEG),[17] and small $A\beta_{1-40}$ protofibrils (PDB codes: 2LMN and 2LMO),[18] where the structure was based on a ssNMR model. In both structures, the N-terminal coordinates, residues 1−16 for the former and 1−8 for the latter structure, are missing due to disorder. We used the $A\beta_{1-16}$ coordinates, in the absence of Zn^{2+} (PDB code: 1ZE7),[19] for the missing portions of the peptides. For each combination of the N-terminal structure with the U-shaped motifs, two $A\beta_{1-42}$ conformers were generated.[6c,d,8] Conformer 1 has a turn at Ser26-Ile31, and conformer 2 at Asp23-Gly29. In the latter conformer, two C-terminal residues, Ile41 and Ala42, were added to create $A\beta_{1-42}$. To simulate pE, we removed the first two residues, Asp1 and Ala2, from each conformer and converted Glu3 into pE3, generating $A\beta_{pE3-42}$. Because the standard CHARMM[20] force field does not provide a force field for pE, we first created the pE molecular topology using the Avogadro software.[21] Then, we calculated partial charges, bond lengths, angles, and torsional angles for the atoms in the pE residue using the Gaussian09 program[22] on a Biowulf cluster at the NIH. The calculated parameters can be directly adopted in the CHARMM[20] program.

Two $A\beta_{pE3-42}$ conformers, each derived from the wild-type (WT) $A\beta_{1-42}$ conformers with different turns, still retain the U-shaped structure with the β-strand-turn-β-strand motif. To construct $A\beta_{pE3-42}$ barrel structures, we inclined $A\beta_{pE3-42}$ monomers ∼37° relative to the pore axis;[7e] then, an 18-fold rotational symmetry operation was performed with respect to the pore axis creating an 18-mer $A\beta_{pE3-42}$ barrel (Figure 1). We modeled Aβ barrels with the β-sheet structure by mimicking naturally occurring β-barrels observed in transmembrane proteins that are found frequently in the outer membranes of bacteria, mitochondria, and chloroplasts. The β-barrel motif is a large β-sheet composed of an even number of β-strands. Some known structures of β-barrel membrane proteins have β-strands ranging in size from 8 to 22.[23] We modeled 18-mer Aβ barrels, with 18 β-strands enclosing the solvated pore. This number is also in the range of the number of β-strands for natural β-barrels ranging from 8 to 22, which can form a β-barrel motif. Our previous simulations for Aβ channels indicate that different numbers of Aβ monomers could produce channels with different outer and pore dimensions.[2b,6c,d,7c−e,8a,24] We found that Aβ channels obtained a preferred size range of 16−24 β-strands lining the pores.[7c,d] This range was also found to hold for other toxic β-sheet channels: K3 channels with 24 β-strands,[25] 18- and 24-mer hIAPP channels,[26] PG-1 channels with 16−20 β-strands,[27] and MAX channels with 20 β-strands.[28] In agreement with AFM data, these channels have outer and pore dimensions within the range found with AFM. In this work, the outer/pore diameters of the 18-mer $A\beta_{pE3-42}$ barrels are in good agreement with the experimental AFM ranges[6b] and the computational 18-mer wild-type Aβ barrels.[6c,8a] The AFM experiments provide images of channels with a wide variety of sizes and shapes, but simulated Aβ barrels are limited to cover all ranges of channel sizes that are imaged by AFM.

To obtain a lipid bilayer, we constructed a unit cell containing two layers of lipids. In the middle of the unit cell, lipid molecules were randomly selected from the library of the preequilibrated state and replaced by pseudo vdW spheres at the positions of the lipid headgroups, constituting the lipid bilayer topology.[29] For a given number of lipid molecules, the optimal value of lateral cell dimensions can be determined. An anionic lipid bilayer composed of DOPS and POPE with a mole ratio 1:2, containing a total of 420 lipids, constitutes the unit cell with TIP3P waters added at both sides. Updated CHARMM[20] all-atom additive force field for lipids (C36)[30] and the modified TIP3P water model[31] were used to construct the set of starting points and to relax the systems to a production-ready stage. The system contains Mg^{2+}, K^+, Ca^{2+}, and Zn^{2+} at the same concentration of 25 mM to satisfy a total cation concentration near 100 mM. The bilayer system containing an $A\beta_{pE}$ barrel, lipids, salts, and water has almost 200 000 atoms. We generated at least 10 different initial configurations for each

dx.doi.org/10.1021/jp5040954 | J. Phys. Chem. B 2014, 118, 7335−7344

conformer $A\beta_{pE3-42}$ barrel for the relaxation process to obtain the best initial configuration for a starting point. In the pre-equilibrium stages, a series of minimizations was performed for the initial configurations to remove overlaps of the alkane chains in the lipids and to gradually relax the solvents around the harmonically restrained peptides. The initial configurations were gradually relaxed through dynamic cycles with electrostatic cutoffs (12 Å). The harmonic restraints were gradually diminished with the full Ewald electrostatics calculation and constant temperature (Nosé–Hoover) thermostat/barostat at 303 K. For t < 30 ns, our simulation employed the NPAT (constant number of atoms, pressure, surface area, and temperature) ensemble with a constant normal pressure applied in the direction perpendicular to the membrane. After t = 30 ns, the simulations employed the NPT ensemble. Production runs of 100 ns for the starting points with the NAMD code[32] were performed on a Biowulf cluster at the NIH. Averages were taken after 30 ns, discarding initial transients. Analysis was performed with the CHARMM programming package.[20]

RESULTS

Pore Activity. PLB electrical recording data demonstrate that $A\beta_{pE3-42}$ peptides induce spontaneous pore activity through lipid membranes presenting the general features observed for $A\beta_{1-42}$ pores (Figure 2). At a concentration of 10 μM and at

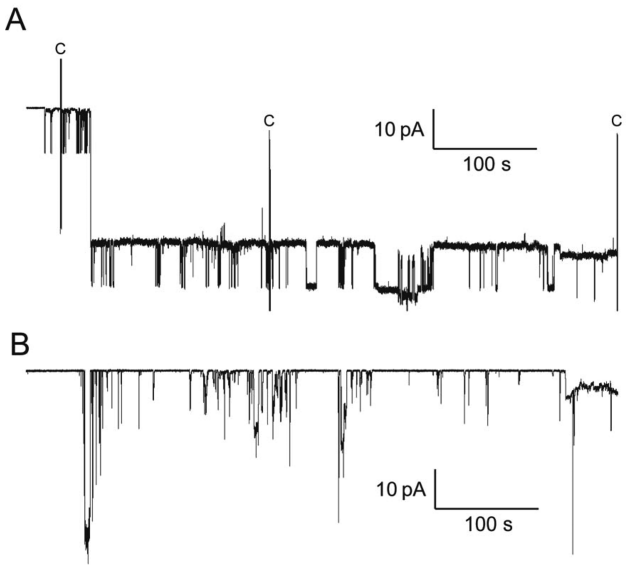

Figure 2. $A\beta_{pE3-42}$ and $A\beta_{1-42}$ produce pore activity in anionic lipid membranes. Representative traces for the activity of (A) $A\beta_{pE3-42}$ and (B) $A\beta_{1-42}$ pores in stable membrane recording. These types of traces were common to both membranes. The activity seen in both membranes, namely step, spike, and burst behavior is characteristic of amyloid ion channels. Bilayers were formed by the painted technique using 1:1 (w/w) mixture of DOPS/POPE. Both sides of the bilayer chamber contained as electrolyte 150 mM KCl, 1 mM $MgCl_2$, and 10 mM HEPES (pH 7.4). −50 mV bias potential is applied.

constant voltage both peptides show stepwise changes in the current flowing through the membrane (Figure 2A), characteristic of the opening and closing of ion channels. However, unlike ion channels that have regulated activity and possess integer values of a unitary conductance, amyloid pores are not regulated and present multiple conductance values due to the different number of monomers composing the pore and membrane–channel interaction dynamics.[7c] The multilevel conductance seen here in both $A\beta_{pE3-42}$ and $A\beta_{1-42}$ is a hallmark of amyloid pores.[6b]

For both peptides, two distinct types of activity were observed. The first, as seen in Figure 2, was characterized by stable, long recording times (>30 min) following the first onset of activity. The second type of activity was characterized by ionic conduction through the membrane that grows rapidly in an exponential-like fashion (Figure 3A). When present, this

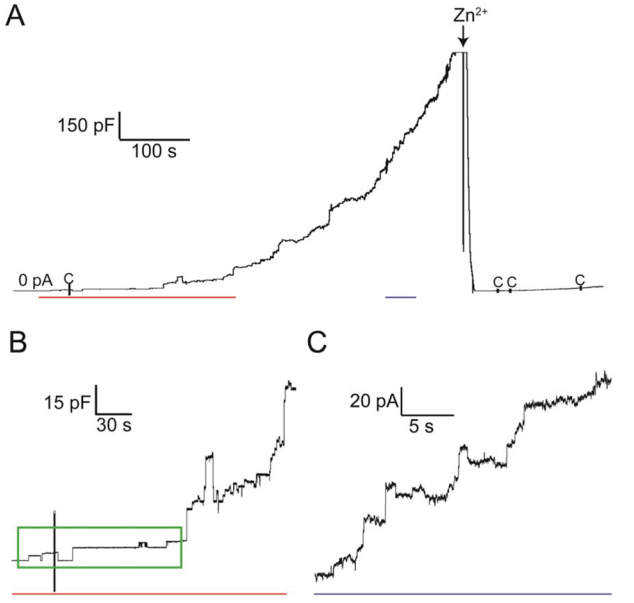

Figure 3. "Exponential" current growth of $A\beta_{pE3-42}$. A +50 mV bias potential is applied. This type of membrane activity was observed in 50% of $A\beta_{pE3-42}$ membranes and 33% of $A\beta_{1-42}$ membranes. (A) The current across the membrane increased rapidly upon disruption of the membrane, exceeding the 1.1 nA saturation current of our amplifier. Addition of Zn^{2+} ions rapidly inhibits $A\beta_{pE3-42}$ activity. (B) Enlargement of the time period indicated by the red line. The transition from stable step behavior to "exponential" growth is highlighted. An abrupt increase in the membrane conductivity due to the opening of a large single pore or several pores simultaneously leads to the opening of several pores in a cascade-like fashion. (C) Clear step behavior is still observed during exponential current growth (region indicated by the short blue line an A). A mixed mechanism involving both channel activity and nonspecific leakage is likely involved.

"exponential" phase began within 20 min of the first observed activity and typically led to current saturation of the amplifier within 10 min. This type of growth was seen in 50% (3/6) of $A\beta_{pE3-42}$ and 33% (2/6) of $A\beta_{1-42}$ membranes (Table 1). At first, only a few pores open (Figure 3B), and the membrane stays in the same conductive state for several 10s of seconds (region inside green rectangle). However, after an abrupt increase in the membrane conductivity due to the opening of a large single pore or several pores simultaneously, the activity is characterized by several short small steps only a few seconds long, suggestive of the opening of several pores in a cascade-like fashion. Despite this rapid growth, discrete steps indicative of pore activity are still clearly observed (Figure 3C). In addition, similar to $A\beta_{1-42}$, $A\beta_{pE3-42}$ pores are voltage-independent and can be blocked by Zn^{2+} (Figure 3A).

Although the overall characteristics of the membrane activity induced by $A\beta_{pE3-42}$ and $A\beta_{1-42}$ pores are similar, distinct

dx.doi.org/10.1021/jp5040954 | J. Phys. Chem. B 2014, 118, 7335–7344

Table 1. Summary of Characteristic Parameters of $A\beta_{pE3-42}$ and $A\beta_{1-42}$ Electrical Activity in Anionic Membranes Showing a Greater Percentage of Activity at Higher Conductance Values, in Particular, in the 100−200 pS Range, As Well As a Longer Lag Period between the Addition of Peptide and the First Observed Activity

peptide	no. of membranes	total events	time to first activity (mean ± SD) (min)	% of membranes with apparent exponential current growth	% event 0−100 pS average conductance	% event 100−200 pS average conductance	% event >200 pS average conductance
$A\beta_{1-42}$	6	1192	31.6 ± 25.7	50	90.77%	4.95%	4.28%
					33.25 ± 25.35 pS	140.92 ± 27.05 pS	362.43 ± 143.82 pS
$A\beta_{pE3-42}$	5	1400	98.2 ± 68.5	33.33	73.98%	20.87%	5.15%
					34.58 ± 24.28 pS	158.85 ± 24.43 pS	436.97 ± 139.59 pS

differences are present. Table 1 displays the characteristic parameters observed for the electrical activity of both $A\beta_{pE3-42}$ and $A\beta_{1-42}$. The onset of $A\beta_{1-42}$ activity in PLB can be observed as soon as several minutes following peptide addition into the chamber and was typically seen within ∼60 min post-addition with an average of 31.6 ± 25.7 min. $A\beta_{pE3-42}$ demonstrated a significantly longer ($p < 0.05$ for a one-tail t test) and more variable lag time, with an average of 98.2 ± 68.5 min.

We next examined whether there was a difference between $A\beta_{pE3-42}$ and $A\beta_{1-42}$ channel conductances. Figure 4 shows the

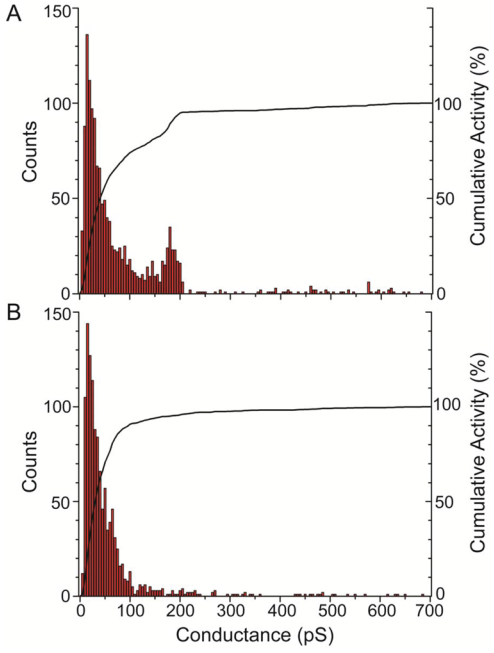

Figure 4. Histogram analysis of (A) $A\beta_{pE3-42}$ and (B) $A\beta_{1-42}$ conductances shows that there is an increased propensity for higher conductance events for $A\beta_{pE3-42}$. Both histograms are binned at 5 pS. Solid lines plot the cumulative percentage of total events. Both sets of conductances can be sorted into three groups; < 100 pS, 100−200 pS and >200 pS, as shown in Table 1. $A\beta_{pE3-42}$ presents significantly more events than $A\beta_{1-42}$ in the 100−200 pS interval. Data sample size was 1400 for $A\beta_{pE3-42}$ and 1192 for $A\beta_{1-42}$. Data were collected in the ±50 mV range, with peptide at a concentration of 10 μM. The electrolyte used was 150 mM KCl, 1 mM $MgCl_2$, and 10 mM HEPES (pH 7.4). Bilayers were made by the painted technique with DOPS/POPE lipids dissolved in heptane.

histogram distribution of single-channel conductances calculated from both step and spike activity. The histograms show that the conductances can be sorted into three groups that demonstrate a shift toward higher conductances for $A\beta_{pE3-42}$ pores (Figure 4A) compared with $A\beta_{1-42}$ (Figure 4B). The first group of conductances, below 100 pS, consisted of 74% of $A\beta_{pE3-42}$ and 91% of $A\beta_{1-42}$ events. The second group is between 100 and 200 pS and, significantly, shows a second peak of activity for $A\beta_{pE3-42}$ that is absent for $A\beta_{1-42}$. While 21% of the events fall in this range for $A\beta_{pE3-42}$, only 5% of $A\beta_{1-42}$ events are in this range. The third grouping shows similar rates of sparse activity greater than 200 pS (5 and 4% for $A\beta_{pE3-42}$ and $A\beta_{1-42}$, respectively). While the percentage of activity in the high conductivity range is similar, close inspection of the histogram shows higher conductances for $A\beta_{pE3-42}$ in this region. (Note the additional grouping around 600 pS.) Table 1 shows that the average conductance in this third region is ∼20% higher for $A\beta_{pE3-42}$. These results show an overall trend for higher $A\beta_{pE3-42}$ conductance, which could have relevance to the $A\beta_{pE3-42}$ toxicity mechanism.

$A\beta_{pE3-42}$ Barrel Conformations in the Lipid Bilayer. We performed 100 ns all-atom MD simulations on $A\beta_{pE3-42}$ barrels embedded in an anionic lipid bilayer composed of DOPS/POPE (mole ratio 1:2). The $A\beta_{pE3-42}$ barrels comprising two different U-shaped conformers were initially preassembled as an annular shape. The initial annular conformation is gradually lost via relaxation of the lipid bilayer, and no immediate peptide dissociation in the barrels was observed (Figure S1 of the Supporting Information). The U-shaped portions of the $A\beta_{pE}$ barrels (residues 15−42 and 11−42 for the conformer 1 and 2 $A\beta_{pE3-42}$ barrels, respectively; see peptide topologies in Figure 1), which mostly include membrane embedded portions, reach equilibration after the initial transient state, while the extramembranous N-termini of the peptides (residues 3−14 and 3−10 for the conformer 1 and 2 $A\beta_{pE3-42}$ barrels, respectively) are disordered (Figure S2 of the Supporting Information). Small fluctuations in the pore and C-terminal strands in the lipid bilayer retain the U-shaped peptide motif in the $A\beta_{pE3-42}$ barrels (Figure S3 of the Supporting Information). In our simulations, the $A\beta_{pE3-42}$ peptide also presents heterogeneity in barrel conformations (Figure 5), as observed in the WT $A\beta_{1-42}$[6c,d] and mutant[8,33] $A\beta$ barrels. The outer diameters for the membrane embedded portion are ∼7.6 and ∼7.1 nm for the conformer 1 and 2 $A\beta_{pE3-42}$ barrels, respectively. The averaged pore diameters are ∼2.2 and ∼1.9 nm for the conformer 1 and 2 $A\beta_{pE3-42}$ barrels, respectively. Both outer/pore diameters of $A\beta_{pE3-42}$ barrel are in the range of the WT barrel.[6c,d,24b]

Unlike the WT $A\beta_{1-42}$ barrels, where the N-terminal strands normally reside in the bulk water area (Figure S4 of the Supporting Information), the pE3 N-termini of $A\beta_{pE3-42}$ barrels tend to retreat to the lipid hydrophobic core due to the hydrophobicity of the lactam ring. To locate the pE3 residue across the bilayer, we calculated the probability distributions for pE3 as well as few selected charged groups in the barrels (Figure 6). The distribution curves for pE3 spanning the interior of the lipid bilayer indicate that several pE3 termini interact with the lipid hydrophobic tails. The interaction energy

dx.doi.org/10.1021/jp5040954 | J. Phys. Chem. B 2014, 118, 7335−7344

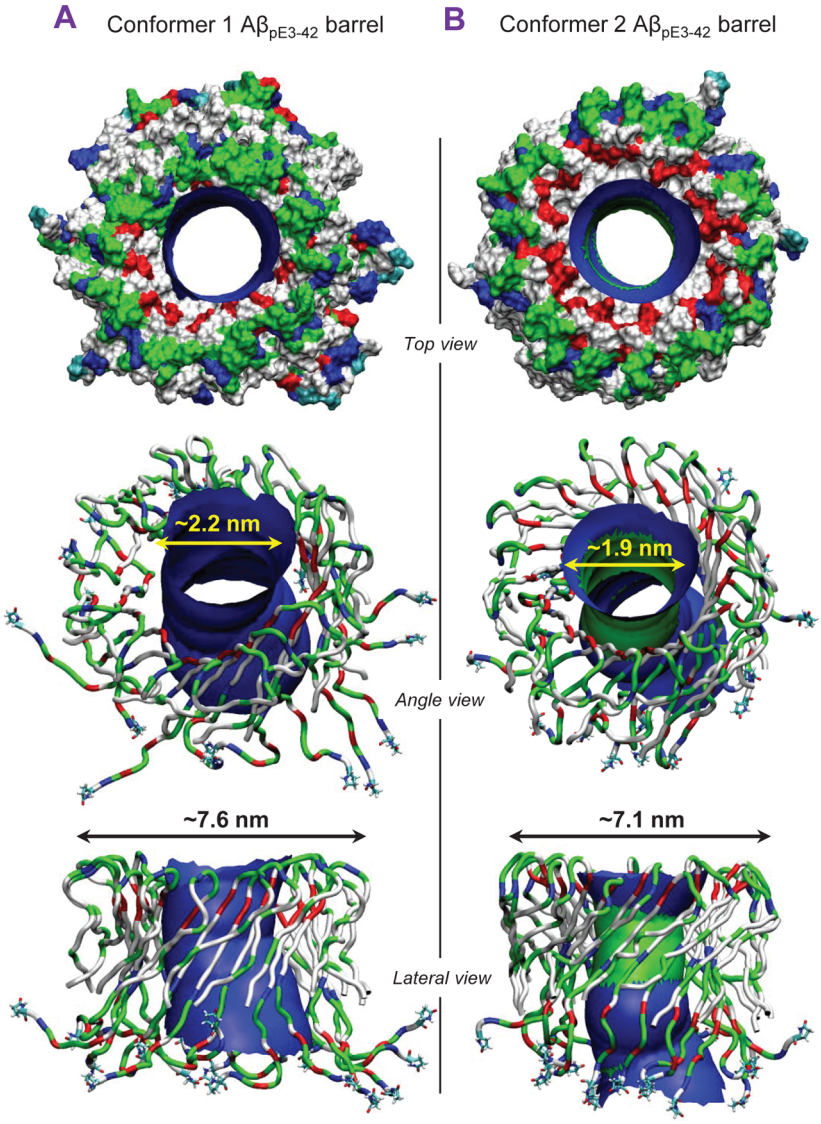

Figure 5. Averaged pore structures calculated with HOLE[38] embedded in the average barrel conformations during the simulations for the (A) conformer 1 and (B) conformer 2 Aβ_{pE3-42} barrels. In the barrel structures with the surface (top view) and the ribbon representations (angle and lateral views), hydrophobic, polar/Gly, positively charged, and negatively charged residues are colored white, green, blue, and red, respectively. For the pore structures, red denotes pore diameter of d < 1.4 nm, green denotes pore diameter in the range, 1.4 nm ≤ d ≤ 2.0 nm, and blue denotes pore diameter of d > 2.0 nm.

of the pE3 residue with lipids shows strong attraction for several pE3 N-termini (blue bars in Figure S5 of the Supporting Information), while no strong lipid interactions of the standard N-termini were observed in the WT Aβ_{1-42} and mutant barrels.[6c,d,8,33] Relocating the pE3 N-termini into the lipid hydrophobic core significantly reduces the fluctuations of the N-terminal portions of barrels at the lower bilayer leaflet, further stabilizing the barrel conformation. With the pE3 anchoring in the membrane, the Aβ_{pE3-42} barrel would provide a clear channel mouth at the lower bilayer leaflet and hence yield a wide-open water pore for ion leakage, suggesting that Aβ_{pE3-42} pores may lead to high ion conductance.

To observe ion activity in the Aβ_{pE3-42} pores, we calculated the probability distribution for ions across the bilayer (Figure S6 of the Supporting Information). Peaks in the distribution curves reflect the highly populated ion binding sites in the pore. The locations of ion binding sites in each conformer Aβ_{pE3-42} barrel are similar to those of each corresponding conformer of WT Aβ_{1-42} barrels because both barrels share the same U-shaped motif in the lipid bilayer. To observe ion fluctuation across the pore, we calculated the change in total charge in the pore as a function of the simulation time (Figure 7). Two selected pore lengths along the pore axis, −1.0 < z < 1.0 nm and −1.8 < z < 1.8 nm, were used in the calculation. These pore lengths ensure that the charge fluctuations exclude a contribution of ion interactions with the lipid head groups. For |z| < 1.0 nm, the pore of the Aβ_{pE3-42} barrel conformer 1 exhibits larger charge fluctuations than the conformer 2 barrel, because the Glu22 cationic binding site is located at z = ∼0.6 nm, attracting more cations into the pore. For the conformer 2 Aβ_{pE3-42} barrel, the Glu22 cationic binding site is located at z = ∼1.8 nm near the channel mouth (as indicated by Ca^{2+} peak at z = ∼1.8 nm in Figure S6B of the Supporting Information). To correlate these charge fluctuations with experimental ion conductance, we calculated the maximum conductance, g_{max},[34] representing the ion transport, which can be described as

dx.doi.org/10.1021/jp5040954 | J. Phys. Chem. B 2014, 118, 7335−7344

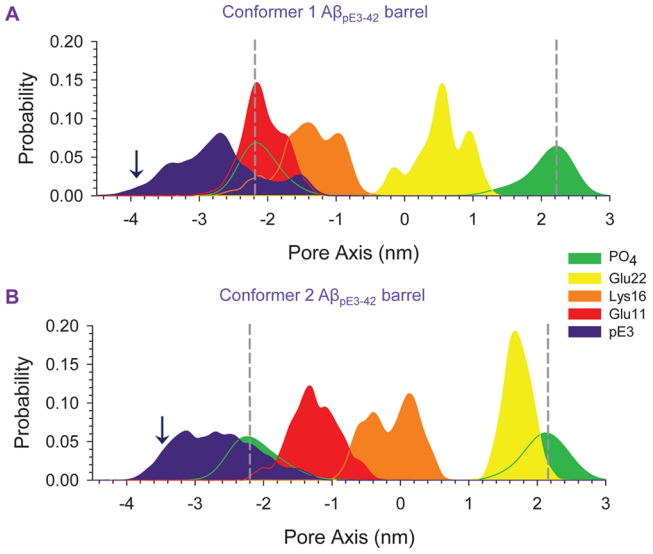

Figure 6. Probability distribution functions for pE3 and selected charged residues, pE3 (purple), Glu11 (red), Lys16 (orange), and Glu22 (yellow), and for the phosphate group of lipid head, PO_4 (green), as a function of the distance along the pore center axis for the (A) conformer 1 and (B) conformer 2 $A\beta_{pE3-42}$ barrels. Dotted lines indicate the locations of bilayer surfaces. Initial locations of pE3 are marked by arrows.

$$g_{max} = \frac{q_e^2}{k_B T L^2} \langle D(z) e^{G_{PMF}(z)/k_B T} \rangle^{-1} \langle e^{-G_{PMF}(z)/k_B T} \rangle^{-1} \quad (1)$$

where q_e is the elementary charge, k_B denotes the Boltzmann's constant, T is the simulation temperature, and L represents the pore length of 36 Å. In the bracket, $D(z)$ and $G_{PMF}(z)$ denote the 1-D diffusion coefficient and the 1-D potential of mean force for ions, respectively. For Mg^{2+}, K^+, Ca^{2+}, and Zn^{2+}, the maximum conductances are 667, 338, 115, 155 pS and 137, 271, 92, 89 pS in the pores of conformers 1 and 2 $A\beta_{pE3-42}$ barrels, respectively. Averaged maximum conductances for ions are relatively higher than those calculated for the WT $A\beta_{1-42}$ barrels.[6d]

DISCUSSION

We have shown that the toxic pE-modified $A\beta$ peptides produce pore activity in DOPS/POPE anionic membranes. These pores demonstrate similar activity characteristics (heterogeneous step, spike and burst conductance, Zn^{2+} blockage) as $A\beta_{1-42}$ pores as well as other previously studied pores of the $A\beta$ family. However, there are also some significant differences. The onset of $A\beta_{pE3-42}$ pore activity is generally delayed, but once started, $A\beta_{pE3-42}$ pores show increased propensity for larger conductance events compared with $A\beta_{1-42}$ pores, particularly in the 100−200 pS range (Figure 4). Structurally, the lactam ring of $A\beta_{pE}$ peptides induces a change in the conformation of the N-terminal strands of the $A\beta_{pE3-42}$ pores. While the N-terminal strands of $A\beta_{1-42}$ pores normally reside in the bulk water region, the N-termini of $A\beta_{pE}$ pores tend to reside in the hydrophobic lipid core, providing the $A\beta_{pE3-42}$ pores with higher stability.

The longer times required for the onset of $A\beta_{pE3-42}$ pore activity are tentatively attributed to (i) the higher hydrophobicity of $A\beta_{pE3-42}$, which decreases the attractive charge-dipole interactions with the zwitterionic lipid heads, thus also decreasing the number of adsorbed $A\beta_{pE3-42}$ oligomers available

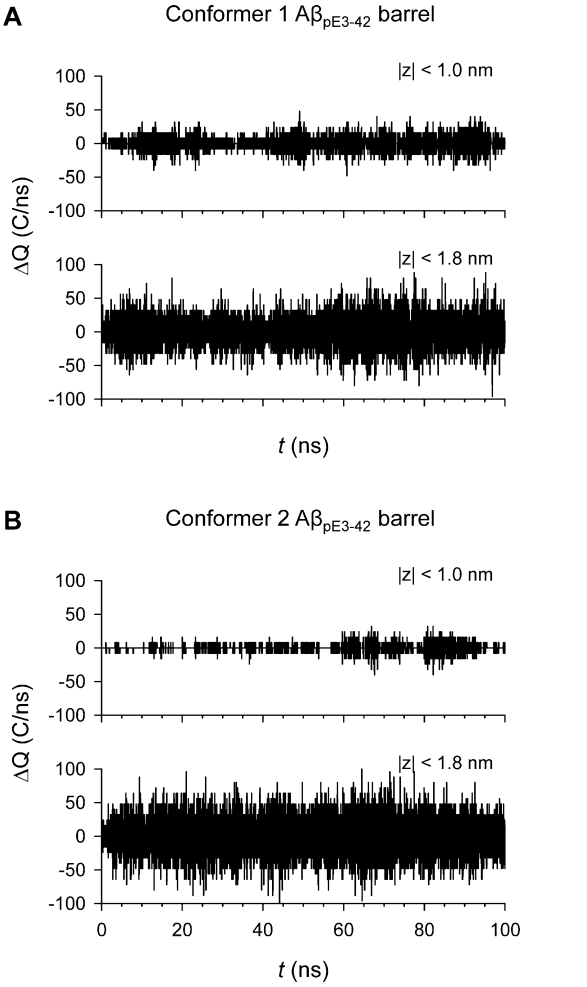

Figure 7. Change in total charge in the pore as a function of the simulation time for the (A) conformer 1 and (B) conformer 2 $A\beta_{pE3-42}$ barrels. The pore heights with cutoff along the pore axis, $-1.0 < z < 1.0$ nm and $-1.8 < z < 1.8$ nm were used.

for subsequent membrane insertion, and (ii) the possible longer times required for pores to assemble in the membrane. Our PLB data demonstrate that the ionic current produced by $A\beta_{pE3-42}$ pores can rapidly rise to levels potentially toxic for cells. Following pore formation, cytotoxicity is produced by an abrupt change in cell ionic concentration. According to early estimations,[5a,b] a single pore with a gigantic 4 nS conductance can produce a change of 10 μM/s in internal Na^+ concentration, producing loss of cell homeostasis in seconds. While no single catastrophic event of this nature was observed (Figure 4), the summation of smaller ionic conductance events can have a similar toxic effect. $A\beta_{pE3-42}$ has been shown to be more cytotoxic than $A\beta_{1-42}$ in vitro.[11,35] We showed that $A\beta_{pE3-42}$ shows a greater propensity for higher conductance values when compared with $A\beta_{1-42}$. This would lead to a more prevalent and rapid dysregulation of cellular ionic homeostasis for $A\beta_{pE3-42}$, thus suggesting increased cytotoxic properties of $A\beta_{pE3-42}$ pores.

The pore structures found for $A\beta_{pE3-42}$ had characteristics and dimensions in accordance with the pores previously reported. Pore structures have been characterized by AFM and modeled using MD simulations for several $A\beta$ peptides. Our previous studies indicate that full-length $A\beta_{1-40/42}$,[6] certain $A\beta$ mutants,[6b,8a] $A\beta$ fragments,[2b,5j,7b−e] as well as other amyloid-

dx.doi.org/10.1021/jp5040954 | J. Phys. Chem. B 2014, 118, 7335−7344

s[6a,b,25,27a,36] form heterogeneous pore structures showing 4−6 subunits and shapes varying from rectangular to hexagonal. Our MD simulations suggest similar pore sizes for both peptides but increased stability of the $A\beta_{pE3\text{-}42}$ pores inserted in DOPS/POPE membranes. Stability in the membrane is likely more important for the formation and longevity of the larger pores with conductances in the 100−200 pS range. As a result, $A\beta_{pE3\text{-}42}$ pores with conductances in this range have a higher population than $A\beta_{1\text{-}42}$ pores (Figure 4). Pores with conductances >200 pS likely have similar and fast decay rates for $A\beta_{pE3\text{-}42}$ and $A\beta_{1\text{-}42}$, and thus both populations are similarly low, although still somewhat larger for $A\beta_{pE3\text{-}42}$. Such a scenario would also correlate with the greater in vitro cytotoxicity observed for $A\beta_{pE3\text{-}42}$ peptides.

The energy of a pore according to the continuum model is[37]

$$E = \gamma 2\pi r - \sigma \pi r^2 \quad (2)$$

where r is the pore radius, γ is the line tension at the pore edge, and σ is the surface tension of the membrane. Our MD results indicate that $A\beta_{pE3\text{-}42}$ and $A\beta_{1\text{-}42}$ pores have similar diameters and general characteristics, while the main difference is the retreat of the N-termini of $A\beta_{pE3\text{-}42}$ into the hydrophobic lipid core. Therefore, this reconfiguration of the N-termini likely decreases the line tension of $A\beta_{pE3\text{-}42}$ pores, minimizing their pore energy and rendering them more stable.

Our results suggest potential mechanisms of cellular disruption. The "exponential" growth of the current, seen in Figure 3, would lead to rapid cell death and was observed in 50% (3/6) of the $A\beta_{pE3\text{-}42}$ membranes in this study. While pore activity appears to be the only mechanism present during the early stages (green rectangle in Figure 3B), the activity trace suggests that two mechanisms of ionic conductance act simultaneously during exponential saturation: (i) stepwise pore behavior and (ii) nonspecific drift leakage. The nonspecific leakage could be caused by a number of alternative mechanisms leading to Aβ-induced membrane permeability, including carpeting and detergent effects.[9b] The data suggest that a combined mechanism (pore and nonspecific leakage) may be at work during the rapid growth of the "exponential" phase, at least some of the time. It is important to note that similar behavior was also seen for some of the $A\beta_{1\text{-}42}$ membranes. Although this behavior was observed for more membranes with $A\beta_{pE3\text{-}42}$ pores, this difference (Table 1) was not statistically significant to reach conclusions regarding specific $A\beta_{pE3\text{-}42}$ cytotoxity.

CONCLUSIONS

In summary, using PLBs and MD simulations, we have shown that $A\beta_{pE3\text{-}42}$ forms ionic pores in DOPS/POPE lipid bilayers. The activity of these pores follows the same general pattern as $A\beta_{1\text{-}42}$ pores. Significantly, however, $A\beta_{pE3\text{-}42}$ pores display higher conductances than $A\beta_{1\text{-}42}$ pores, in particular, in the 100−200 pS range. In addition, the onset of $A\beta_{pE3\text{-}42}$ pore activity is delayed compared with $A\beta_{1\text{-}42}$ pores. Structurally, $A\beta_{pE3\text{-}42}$ and $A\beta_{1\text{-}42}$ pores have similar dimensions, but the pE3 residue induces a change in the conformation of the N-terminal strands of the $A\beta_{pE3\text{-}42}$ pores. While the N-terminal strands of $A\beta_{1\text{-}42}$ pores normally reside in the bulk water region, the N-termini of $A\beta_{pE}$ pores tend to reside in the hydrophobic lipid core, providing the $A\beta_{pE3\text{-}42}$ pores with higher stability compared with the $A\beta_{1\text{-}42}$ pores. These studies are a first step in understanding the role of pores in the enhanced toxicity attributed to $A\beta_{pE}$ peptides.

ASSOCIATED CONTENT

Supporting Information

Time series of $A\beta_{pE3\text{-}42}$ barrel conformations. Peptide-averaged and residue-averaged RMSDs. Probability distribution functions for selected residues in the wild-type barrels. Interaction energy of pE3 residue with lipids. Probability distribution functions for ions. This material is available free of charge via the Internet at http://pubs.acs.org.

AUTHOR INFORMATION

Corresponding Author

*Tel: 858-822-1322. E-mail: ftarce@ucsd.edu.

Author Contributions

#A.L.G. and H.J. authors contributed equally to this work

Notes

The authors declare no competing financial interest.

ACKNOWLEDGMENTS

We thank Prof. Ratnesh Lal for his insight and support for this work. Support by the National Institutes of Health (R01AG028709) is acknowledged. A.L.G was supported in part by National Institutes of Health Neuroplasticity of Aging Training Grant (T32 AG 000216) and the Howard Hughes Medical Institute Med Into Grad Initiative. This project has been funded in whole or in part with Federal funds from the Frederick National Laboratory for Cancer Research, National Institutes of Health, under contract HHSN261200800001E. This research was supported [in part] by the Intramural Research Program of NIH, Frederick National Lab, Center for Cancer Research. The content of this publication does not necessarily reflect the views or policies of the Department of Health and Human Services, nor does mention of trade names, commercial products, or organizations imply endorsement by the U.S. Government. All simulations had been performed using the high-performance computational facilities of the Biowulf PC/Linux cluster at the National Institutes of Health, Bethesda, MD (http://biowulf.nih.gov).

REFERENCES

(1) (a) Tanzi, R. E.; Bertram, L. Twenty Years Of The Alzheimer's Disease Amyloid Hypothesis: A Genetic Perspective. *Cell* **2005**, *120* (4), 545−555. (b) Iversen, L. L.; Mortishiresmith, R. J.; Pollack, S. J.; Shearman, M. S. The Toxicity In-Vitro Of Beta-Amyloid Protein. *Biochem. J.* **1995**, *311*, 1−16. (c) Jakob-Roetne, R.; Jacobsen, H. Alzheimer's Disease: From Pathology To Therapeutic Approaches. *Angew. Chem., Int. Ed.* **2009**, *48* (17), 3030−3059. (d) Hardy, J.; Selkoe, D. J. Medicine - The Amyloid Hypothesis Of Alzheimer's Disease: Progress And Problems On The Road To Therapeutics. *Science* **2002**, *297* (5580), 353−356. (e) Hardy, J. A.; Higgins, G. A. Alzheimers Disease: The Amyloid Cascade Hypothesis. *Science* **1992**, *256* (5054), 184−185.

(2) (a) Thinakaran, G.; Koo, E. H. Amyloid Precursor Protein Trafficking, Processing, and Function. *J. Biol. Chem.* **2008**, *283* (44), 29615−29619. (b) Jang, H.; Arce, F. T.; Ramachandran, S.; Capone, R.; Azimova, R.; Kagan, B. L.; Nussinov, R.; Lal, R. Truncated B-Amyloid Peptide Channels Provide An Alternative Mechanism For Alzheimer's Disease And Down Syndrome. *Proc. Natl. Acad. Sci. U.S.A.* **2010**, 6538−6543.

(3) (a) Jawhar, S.; Wirths, O.; Bayer, T. A. Pyroglutamate Amyloid-B (Aβ): A Hatchet Man In Alzheimer Disease. *J. Biol. Chem.* **2011**, *286* (45), 38825−38832. (b) Saido, T. C.; Iwatsubo, T.; Mann, D. M. A.; Shimada, H.; Ihara, Y.; Kawashima, S. Dominant And Differential Deposition Of Distinct Beta-Amyloid Peptide Species, A-Beta(N3-(Pe)), In Senile Plaques. *Neuron* **1995**, *14* (2), 457−466.

(4) (a) Saido, T. C.; Yamaoharigaya, W.; Iwatsubo, T.; Kawashima, S. Amino- And Carboxyl-Terminal Heterogeneity Of Beta-Amyloid Peptides Deposited In Human Brain. *Neurosci. Lett.* **1996**, *215* (3), 173−176. (b) Piccini, A.; Russo, C.; Gliozzi, A.; Relini, A.; Vitali, A.; Borghi, R.; Giliberto, L.; Armirotti, A.; D'Arrigo, C.; Bachi, A.; et al. Beta-Amyloid Is Different In Normal Aging And In Alzheimer Disease. *J. Biol. Chem.* **2005**, *280* (40), 34186−34192. (c) Tabaton, M.; Piccini, A. Role Of Water-Soluble Amyloid-Beta In The Pathogenesis Of Alzheimer's Disease. *Int. J. Exp. Pathol.* **2005**, *86* (3), 139−145.

(5) (a) Arispe, N.; Pollard, H. B.; Rojas, E. Giant Multilevel Cation Channels Formed By Alzheimer Disease Amyloid Beta-Protein [A Beta P-(1−40)] In Bilayer Membranes. *Proc. Natl. Acad. Sci. U.S.A.* **1993**, *90* (22), 10573−10577. (b) Arispe, N.; Rojas, E.; Pollard, H. B. Alzheimer Disease Amyloid B Protein Forms Calcium Channels In Bilayer Membranes: Blockade By Tromethamine And Aluminum. *Proc. Natl. Acad. Sci. U.S.A.* **1993**, *90* (2), 567−571. (c) Capone, R.; Quiroz, F. G.; Prangkio, P.; Saluja, I.; Sauer, A. M.; Bautista, M. R.; Turner, R. S.; Yang, J.; Mayer, M. Amyloid-Beta-Induced Ion Flux In Artificial Lipid Bilayers And Neuronal Cells: Resolving A Controversy. *Neurotoxic. Res.* **2009**, *16* (1), 1−13. (d) Prangkio, P.; Yusko, E. C.; Sept, D.; Yang, J.; Mayer, M. Multivariate Analyses Of Amyloid-Beta Oligomer Populations Indicate A Connection Between Pore Formation And Cytotoxicity. *PLoS One* **2012**, *7*, 10. (e) Demuro, A.; Smith, M.; Parker, I. Single-Channel Ca^{2+} Imaging Implicates Aβ1−42 Amyloid Pores In Alzheimer's Disease Pathology. *J. Cell Biol.* **2011**, *195* (3), 515−524. (f) Kagan, B. L.; Azimov, R.; Azimova, R. Amyloid Peptide Channels. *J. Membr. Biol.* **2004**, *202* (1), 1−10. (g) Kagan, B. L.; Hirakura, Y.; Azimov, R.; Azimova, R.; Lin, M. C. The Channel Hypothesis Of Alzheimer's Disease: Current Status. *Peptides* **2002**, *23* (7), 1311−1315. (h) Kim, H. Y.; Cho, M. K.; Kumar, A.; Maier, E.; Siebenhaar, C.; Becker, S.; Fernandez, C. O.; Lashuel, H. A.; Benz, R.; Lange, A.; et al. Structural Properties Of Pore-Forming Oligomers Of Alpha-Synuclein. *J. Am. Chem. Soc.* **2009**, *131* (47), 17482−17489. (i) Jang, H.; Connelly, L.; Arce, F. T.; Ramachandran, S.; Lal, R.; Kagan, B.; Nussinov, R. Alzheimer's Disease: Which Type Of Amyloid-Preventing Drug Agents To Employ? *Phys. Chem. Chem. Phys.* **2013**, *15*, 8868−8877. (j) Jang, H.; Connelly, L.; Arce, F. T.; Ramachandran, S.; Kagan, B. L.; Lal, R.; Nussinov, R. Mechanisms For The Insertion Of Toxic, Fibril-Like Beta-Amyloid Oligomers Into The Membrane. *J. Chem. Theory Comput.* **2013**, *9* (1), 822−833.

(6) (a) Lin, H. A. I.; Bhatia, R.; Lal, R. Amyloid B Protein Forms Ion Channels: Implications For Alzheimer's Disease Pathophysiology. *FASEB J.* **2001**, *15* (13), 2433−2444. (b) Quist, A.; Doudevski, I.; Lin, H.; Azimova, R.; Ng, D.; Frangione, B.; Kagan, B.; Ghiso, J.; Lal, R. Amyloid Ion Channels: A Common Structural Link For Protein-Misfolding Disease. *Proc. Natl. Acad. Sci. U.S.A.* **2005**, *102* (30), 10427−10432. (c) Connelly, L.; Arce, F. T.; Jang, H.; Capone, R.; Kotler, S. A.; Ramachandran, S.; Kagan, B. L.; Nussinov, R.; Lal, R. Atomic Force Microscopy And MD Simulations Reveal Pore-Like Structures Of All-D-Enantiomer Of Alzheimer's B-Amyloid Peptide: Relevance To The Ion Channel Mechanism Of AD Pathology. *J. Phys. Chem. B* **2012**, *116* (5), 1728−1735. (d) Capone, R.; Jang, H.; Kotler, S. A.; Connelly, L.; Arce, F. T.; Ramachandran, S.; Kagan, B. L.; Nussinov, R.; Lal, R. All-D-Enantiomer Of Beta-Amyloid Peptide Forms Ion Channels In Lipid Bilayers. *J. Chem. Theory Comput.* **2012**, *8* (3), 1143−1152.

(7) (a) Lin, M. C. A.; Kagan, B. L. Electrophysiologic Properties Of Channels Induced By A Beta 25−35 In Planar Lipid Bilayers. *Peptides* **2002**, *23* (7), 1215−1228. (b) Arce, F. T.; Jang, H.; Ramachandran, S.; Landon, P. B.; Nussinov, R.; Lal, R. Polymorphism Of Amyloid B Peptide In Different Environments: Implications For Membrane Insertion And Pore Formation. *Soft Matter* **2011**, *7* (11), 5267−5273. (c) Jang, H.; Arce, F. T.; Capone, R.; Ramachandran, S.; Lal, R.; Nussinov, R. Misfolded Amyloid Ion Channels Present Mobile B-Sheet Subunits In Contrast To Conventional Ion Channels. *Biophys. J.* **2009**, *97* (11), 3029−3037. (d) Jang, H.; Arce, F. T.; Ramachandran, S.; Capone, R.; Lal, R.; Nussinov, R. Structural Convergence Among Diverse, Toxic B-Sheet Ion Channels. *J. Phys. Chem. B* **2010**, *114* (29), 9445−9451. (e) Jang, H.; Arce, F. T.; Ramachandran, S.; Capone, R.; Lal, R.; Nussinov, R. B-Barrel Topology Of Alzheimer's B-Amyloid Ion Channels. *J. Mol. Biol.* **2010**, *404* (5), 917−934.

(8) (a) Connelly, L.; Jang, H.; Arce, F. T.; Ramachandran, S.; Kagan, B. L.; Nussinov, R.; Lal, R. Effects Of Point Substitutions On The Structure Of Toxic Alzheimer's B-Amyloid Channels: Atomic Force Microscopy And Molecular Dynamics Simulations. *Biochemistry* **2012**, *51* (14), 3031−3038. (b) Connelly, L.; Jang, H.; Teran Arce, F.; Capone, R.; Kotler, S. A.; Ramachandran, S.; Kagan, B. L.; Nussinov, R.; Lal, R. Atomic Force Microscopy And MD Simulations Reveal Pore-Like Structures Of All-D-Enantiomer Of Alzheimer's B-Amyloid Peptide: Relevance To The Ion Channel Mechanism Of AD Pathology. *J. Phys. Chem. B* **2012**, *116* (5), 1728−1735.

(9) (a) Butterfield, S. M.; Lashuel, H. A. Amyloidogenic Protein−Membrane Interactions: Mechanistic Insight From Model Systems. *Angew. Chem., Int. Ed.* **2010**, *49*, 5628−5654. (b) Williams, T. L.; Serpell, L. C. Membrane And Surface Interactions Of Alzheimer's A Beta Peptide - Insights Into The Mechanism Of Cytotoxicity. *FEBS J.* **2011**, *278* (20), 3905−3917.

(10) Sciacca, M. F. M.; Kotler, S. A.; Brender, J. R.; Chen, J.; Lee, D. K.; Ramamoorthy, A. Two-Step Mechanism Of Membrane Disruption By A Beta Through Membrane Fragmentation And Pore Formation. *Biophys. J.* **2012**, *103* (4), 702−710.

(11) Wirths, O.; Breyhan, H.; Cynis, H.; Schilling, S.; Demuth, H. U.; Bayer, T. A. Intraneuronal Pyroglutamate-Abeta 3−42 Triggers Neurodegeneration And Lethal Neurological Deficits In A Transgenic Mouse Model. *Acta Neuropathol.* **2009**, *118* (4), 487−496.

(12) Soderberg, M.; Edlund, C.; Alafuzoff, I.; Kristensson, K.; Dallner, G. Lipid-Composition In Different Regions Of The Brain In Alzheimers-Disease Senile Dementia Of Alzheimers Type. *J. Neurochem.* **1992**, *59* (5), 1646−1653.

(13) Wells, K.; Farooqui, A. A.; Liss, L.; Horrocks, L. A. Neural Membrane Phospholipids In Alzheimer Disease. *Neurochem. Res.* **1995**, *20* (11), 1329−1333.

(14) (a) Nitsch, R. M.; Blusztajn, J. K.; Pittas, A. G.; Slack, B. E.; Growdon, J. H.; Wurtman, R. J. Evidence For A Membrane Defect In Alzheimer-Disease Brain. *Proc. Natl. Acad. Sci. U.S.A.* **1992**, *89* (5), 1671−1675. (b) Svennerholm, L.; Gottfries, C. G. Membrane-Lipids, Selectively Diminished In Alzheimer Brains, Suggest Synapse Loss As A Primary Event In Early-Onset Form (Type-I) And Demyelination In Late-Onset Form (Type-II). *J. Neurochem.* **1994**, *62* (3), 1039−1047.

(15) Mueller, P.; Rudin, D. O.; Tien, H. T.; Wescott, W. C. Reconstitution Of Cell Membrane Structure In Vitro And Its Transformation Into An Excitable System. *Nature* **1962**, *194* (4832), 979−980.

(16) Capone, R.; Jang, H.; Kotler, S. A.; Kagan, B. L.; Nussinov, R.; Lal, R. Probing Structural Features Of Alzheimer's Amyloid-Beta Pores In Bilayers Using Site-Specific Amino Acid Substitutions. *Biochemistry* **2012**, *51* (3), 776−785.

(17) Lührs, T.; Ritter, C.; Adrian, M.; Riek-Loher, D.; Bohrmann, B.; Doeli, H.; Schubert, D.; Riek, R. 3D Structure Of Alzheimer's Amyloid-B(1−42) Fibrils. *Proc. Natl. Acad. Sci. U. S. A.* **2005**, *102* (48), 17342−17347.

(18) Petkova, A. T.; Yau, W. M.; Tycko, R. Experimental Constraints On Quaternary Structure In Alzheimer's B-Amyloid Fibrils. *Biochemistry* **2006**, *45* (2), 498−512.

(19) Zirah, S.; Kozin, S. A.; Mazur, A. K.; Blond, A.; Cheminant, M.; Segalas-Milazzo, I.; Debey, P.; Rebuffat, S. Structural Changes Of Region 1−16 Of The Alzheimer Disease Amyloid B-Peptide Upon Zinc Binding And In Vitro Aging. *J. Biol. Chem.* **2006**, *281* (4), 2151−2161.

(20) Brooks, B. R.; Bruccoleri, R. E.; Olafson, B. D.; States, D. J.; Swaminathan, S.; Karplus, M. Charmm - A Program For Macromolecular Energy, Minimization, And Dynamics Calculations. *J. Comput. Chem.* **1983**, *4* (2), 187−217.

(21) Hanwell, M. D.; Curtis, D. E.; Lonie, D. C.; Vandermeersch, T.; Zurek, E.; Hutchison, G. R. Avogadro: An Advanced Semantic Chemical Editor, Visualization, And Analysis Platform. *J. Cheminform* **2012**, *4* (1), 17.

(22) Frisch, M. J.; Trucks, G. W.; Schlegel, H. B.; Scuseria, G. E.; Robb, M. A.; Cheeseman, J. R.; Scalmani, G.; Barone, V.; Mennucci, B.; Petersson, G. A.; et al. *Gaussian 09*, revision B.01; Gaussian, Inc.: Wallingford CT, 2009.
(23) Schulz, G. E. The Structure Of Bacterial Outer Membrane Proteins. *Biochim. Biophys. Acta* **2002**, *1565* (2), 308−317.
(24) (a) Capone, R.; Jang, H.; Kotler, S. A.; Kagan, B. L.; Nussinov, R.; Lal, R. Probing Structural Features Of Alzheimer's Amyloid-B Pores In Bilayers Using Site-Specific Amino Acid Substitutions. *Biochemistry* **2012**, *51* (3), 776−785. (b) Jang, H.; Teran Arce, F.; Ramachandran, S.; Kagan, B. L.; Lal, R.; Nussinov, R. Disordered Amyloidogenic Peptides May Insert Into The Membrane And Assemble Into Common Cyclic Structural Motifs. *Chem. Soc. Rev.* **2014**, DOI: 10.1039/C3CS60459D. (c) Jang, H.; Zheng, J.; Lal, R.; Nussinov, R. New Structures Help The Modeling Of Toxic Amyloidβ Ion Channels. *Trends Biochem. Sci.* **2008**, *33* (2), 91−100. (d) Jang, H.; Zheng, J.; Nussinov, R. Models Of B-Amyloid Ion Channels In The Membrane Suggest That Channel Formation In The Bilayer Is A Dynamic Process. *Biophys. J.* **2007**, *93* (6), 1938−1949. (e) Jang, H.; Arce, F. T.; Ramachandran, S.; Kagan, B. L.; Lal, R.; Nussinov, R. Familial Alzheimer's Disease Osaka Mutant (ΔE22) B-Barrels Suggest An Explanation For The Different A$\beta_{(1-40/42)}$ Preferred Conformational States Observed By Experiment. *J. Phys. Chem. B* **2013**, *117* (39), 11518−11529.
(25) Mustata, M.; Capone, R.; Jang, H.; Arce, F. T.; Ramachandran, S.; Lal, R.; Nussinov, R. K3 Fragment Of Amyloidogenic Beta(2)-Microglobulin Forms Ion Channels: Implication For Dialysis Related Amyloidosis. *J. Am. Chem. Soc.* **2009**, *131* (41), 14938−14945.
(26) Zhao, J.; Luo, Y.; Jang, H. B.; Yu, X.; Wei, G. H.; Nussinov, R.; Zheng, J. Probing Ion Channel Activity Of Human Islet Amyloid Polypeptide (Amylin). *Biochim. Biophys. Acta, Biomembr.* **2012**, *1818* (12), 3121−3130.
(27) (a) Capone, R.; Mustata, M.; Jang, H.; Arce, F. T.; Nussinov, R.; Lal, R. Antimicrobial Protegrin-1 Forms Ion Channels: Molecular Dynamic Simulation, Atomic Force Microscopy, And Electrical Conductance Studies. *Biophys. J.* **2010**, *98* (11), 2644−2652. (b) Jang, H.; Ma, B.; Lal, R.; Nussinov, R. Models Of Toxic Beta-Sheet Channels Of Protegrin-1 Suggest A Common Subunit Organization Motif Shared With Toxic Alzheimer Beta-Amyloid Ion Channels. *Biophys. J.* **2008**, *95* (10), 4631−4642.
(28) Gupta, K.; Jang, H.; Harlen, K.; Puri, A.; Nussinov, R.; Schneider, J. P.; Blumenthal, R. Mechanism Of Membrane Permeation Induced By Synthetic Beta-Hairpin Peptides. *Biophys. J.* **2013**, *105* (9), 2093−2103.
(29) Woolf, T. B.; Roux, B. Molecular Dynamics Simulation Of The Gramicidin Channel In A Phospholipid Bilayer. *Proc. Natl. Acad. Sci. U.S.A.* **1994**, *91* (24), 11631−11635.
(30) Klauda, J. B.; Venable, R. M.; Freites, J. A.; O'Connor, J. W.; Tobias, D. J.; Mondragon-Ramirez, C.; Vorobyov, I.; Mackerell, A. D.; Pastor, R. W. Update Of The CHARMM All-Atom Additive Force Field For Lipids: Validation On Six Lipid Types. *J. Phys. Chem. B* **2010**, *114* (23), 7830−7843.
(31) Durell, S. R.; Brooks, B. R.; Bennaim, A. Solvent-Induced Forces Between Two Hydrophilic Groups. *J. Phys. Chem.* **1994**, *98*, 2198−2202.
(32) Phillips, J. C.; Braun, R.; Wang, W.; Gumbart, J.; Tajkhorshid, E.; Villa, E.; Chipot, C.; Skeel, R. D.; Kale, L.; Schulten, K. Scalable Molecular Dynamics With NAMD. *J. Comput. Chem.* **2005**, *26*, 1781−1802.
(33) Jang, H.; Teran Arce, F.; Ramachandran, S.; Kagan, B. L.; Lal, R.; Nussinov, R. Familial Alzheimer's Disease Osaka Mutant (Deltae22) Beta-Barrels Suggest An Explanation For The Different Abeta1−40/42 Preferred Conformational States Observed By Experiment. *J. Phys. Chem. B* **2013**, *117* (39), 11518−11529.
(34) Allen, T. W.; Andersen, O. S.; Roux, B. Energetics Of Ion Conduction Through The Gramicidin Channel. *Proc. Natl. Acad. Sci. U.S.A.* **2004**, *101* (1), 117−122.
(35) Nussbaum, J. M.; Schilling, S.; Cynis, H.; Silva, A.; Swanson, E.; Wangsanut, T.; Tayler, K.; Wiltgen, B.; Hatami, A.; Ronicke, R.; Reymann, K.; Hutter-Paier, B.; Alexandru, A.; Jagla, W.; Graubner, S.; Glabe, C. G.; Demuth, H. U.; Bloom, G. S. Prion-Like Behaviour And Tau-Dependent Cytotoxicity Of Pyroglutamylated Amyloid-Beta. *Nature* **2012**, *485* (7400), 651−655.
(36) Jang, H.; Arce, F. T.; Mustata, M.; Ramachandran, S.; Capone, R.; Nussinov, R.; Lal, R. Antimicrobial Protegrin-1 Forms Amyloid-Like Fibrils With Rapid Kinetics Suggesting A Functional Link. *Biophys. J.* **2011**, *100* (7), 1775−1783.
(37) Bleicken, S.; Wagner, C.; Garcia-Saez, A. J. Mechanistic Differences In The Membrane Activity Of Bax And Bcl-Xl Correlate With Their Opposing Roles In Apoptosis. *Biophys. J.* **2013**, *104* (2), 421−431.
(38) Smart, O. S.; Goodfellow, J. M.; Wallace, B. A. The Pore Dimensions Of Gramicidin A. *Biophys. J.* **1993**, *65* (6), 2455−2460.